Electronic Supplementary Information

Surface Amorphized *in-situ* RuO-NiFeOOH/Au Islands for Electrocatalytic Oxygen Evolution Reaction

Karthick Kannimuthu,[1] Pawan Kumar,[1] Pooja Gakhad,[2] Hadi Shaker Shiran,[1] Xiyang Wang,[3] Ali Shayesteh Zeraati,[1] Sangeetha Kumaravel,[4] Shariful Kibria Nabil,[1] Rajangam Vinodh,[1] Md Abdullah Al Bari,[1] Maria Molina,[1] George Shimizu,[1] Yimin A. Wu,[3] Pulickel M. Ajayan,[5] Abhishek Kumar Singh,[2] Soumyabrata Roy,[5,6] and Md Golam Kibria[1]*

[1]*Department of Chemical and Petroleum Engineering, University of Calgary, 2500 University Drive, NW Calgary, Alberta, Canada T2N 1N4.*

[2]*Materials Research Centre, Indian Institute of Science, Bangalore 560 012, India*

[3]*Department of Mechanical and Mechatronics Engineering, Waterloo Institute for Nanotechnology, Materials Interface Foundry, University of Waterloo, Waterloo, Ontario N2L 3G1, Canada*

[4]*Department of Chemistry, Kalasalingam Academy of Research and Education, Srivilliputhur 626126, India.*

[5]*Department of Materials Science and Nanoengineering, Rice University, 6100 Main St., Houston, TX 77030, USA.*

[6]*Department of Sustainable Energy Engineering, Indian Institute of Technology Kanpur, Kanpur, Uttar Pradesh 208016, India*

E-mail: md.kibria@ucalgary.ca

1. Experimental details

2. Figures

Tables

1. Experimental details

1.1 Reagent and materials

Ruthenium trichloride ($RuCl_3.xH_2O$) (99.98 %), Au chloride solution ($HAuCl_4·3H_2O$, ≥99.9% trace metals basis), Nickel foam (NF), Iron nitrate ($Fe(NO_3)_3.9H_2O$ (≥98%), Sodium hypophosphite ($NaH_2PO_2.H_2O$) (≥99%), PMDA (97%), KOH (≥85%), and HPLC grade water were used throughout the experiments.

1.2. Synthesis of Ru-NiFeP/Au by an electrodeposition method

For the synthesis of Au-NF, galvanic replacement technique was employed. NF was initially washed with 3M HCl to exclude the surface oxides. After that, NF piece was added to 50 mL of 34 mg/L of gold (III) chloride at pH~4 buffer and 0.5M NaCl and kept for stirring for 30 min. The prepared Au/NF were used as working electrodes, Ag/AgCl used as a reference and carbon cloth as a counter electrode. To the 5, 10, 15, 20, 25 mmol of $RuCl_3.xH_2O$, 10 mmol $Fe(NO_3)_3.9H_2O$, and 100 mmol $NaH_2PO_2.H_2O$ electrolytes, constant potential of -1.3 V is applied for 300 s. The formed product is named Ru5-NiFeP/Au-NF. Here, NF itself acted as a Ni source. After the deposition, electrodes were washed with DI water several times and dried at room temperature.

1.3. Physical characterization

The crystallinity of the samples was determined using X-ray diffraction (XRD) recorded on a Bruker D8 Discover instrument using Cu-Kα radiation (40 kV, λ = 0.15418 nm) equipped with a LynxEYE 1-dimensional detector. The scan rate of 0.02° is within the 2θ range of 10–90°. The morphology was analyzed by scanning electron microscopy (SEM-EDS) (Phenom proX Desktop). JEOL JEM-ARM200CF S/TEM operating at an acceleration voltage of 200 KeVwas used to acquire high resolution – transmission electron microscopy (HR-TEM) images. X-ray photoelectron spectroscopy (XPS) on an Axis-Ultra, Kratos Analytical instrument and a monochromatic Al-Kα source (photon energy ≈1486.7 eV, source voltage-15 kV, current-10 mA, power-50 W, Rowland circle monochromator) under ultrahigh vacuum ($\sim 10^{-9}$ Torr). The binding energies of all elements were corrected with respect to adventitious carbon peak at 284.6 eV. The *in-situ* Raman spectroscopy was used to investigate changes in the vibrational modes of the electrodes using a Thermo Scientific DXR2 Raman microscope equipped with a 532 nm laser. The crystalline nature of the materials were also studied by synchrotron-based wide-angle X-ray scattering (WAXS) measurement. The WAXS analysis was carried out at 04ID-1 BXDS-WLE, low energy wiggler beamline of Canadian light source (CLS). The energy range for this beamline was 7-22 keV, with a maximum photon flux of 1 x 10^{12} to 5 x 10^{12} photons/s in focus on the sample at 250 mA ring current. The electronic nature of the samples were studied using synchrotron-based soft X-ray absorption spectroscopy (sXAS) and the beamline operating energy range was 3.5–1500 eV, monochromator VLS-PGM, deviation angle 140-176.3º, spectral resolution- 10^4 (E/ΔE) @100eV, 10 µm slit width and spot size 2x 0.2 mm^2. Local chemical environment and co-ordination nature was studied by Hard X-ray Microanalysis (HXMA) beamline of CLS. The energy range for the beamline was 5-40 KeV with a superconducting Wiggler source and photon flux of 1012@12 keV. The spot size was 0.8 x 1.5 mm while the spectral resolution was $1x10^{-4}$.

1.4.Electrochemical OER Studies

Electrocatalytic OER studies were executed in a three-electrode cell in 1M KOH electrolyte. Carbon paper as a counter electrode, Ag/AgCl as a reference electrode and RuNiFeP/Au electrodes acted as working electrodes. Freshly prepared KOH (50 mL) was used to study OER measurements. After 5 CV scans at 100 mV s^{-1} for activation, LSV was carried out at a scan rate of 5 mV s^{-1}. The LSV curves were 50% *iR*-corrected from the R_s values read from the EIS studies. The *in-situ* EIS studies were tested at different applied potential biases with an AC amplitude of 0.005 V in the frequencies range of 100 kHz to 0.1 kHz. Electrochemical active surface area (ECSA) was derived from the C_{dl} method in a non-faradaic region (0-0.1 V vs Ag/AgCl) and calculated from j_a-j_c vs υ. The stability of the electrodes was measured via the galvanostatic method at a constant current density of 100 mA cm^{-2} for 30 h in OER. TOF for OER was calculated using the following formula,

$$TOF = jS/4nF$$

Where, j – current density, S – geometrical surface area, n – active molar sites (from ICP-MS) and F – Faraday constant. The mass activity was calculated using,

Mass activity = Current density (j)/loading (mg). The specific activity of the electrodes was measured by normalizing the current with the calculated ECSA values.

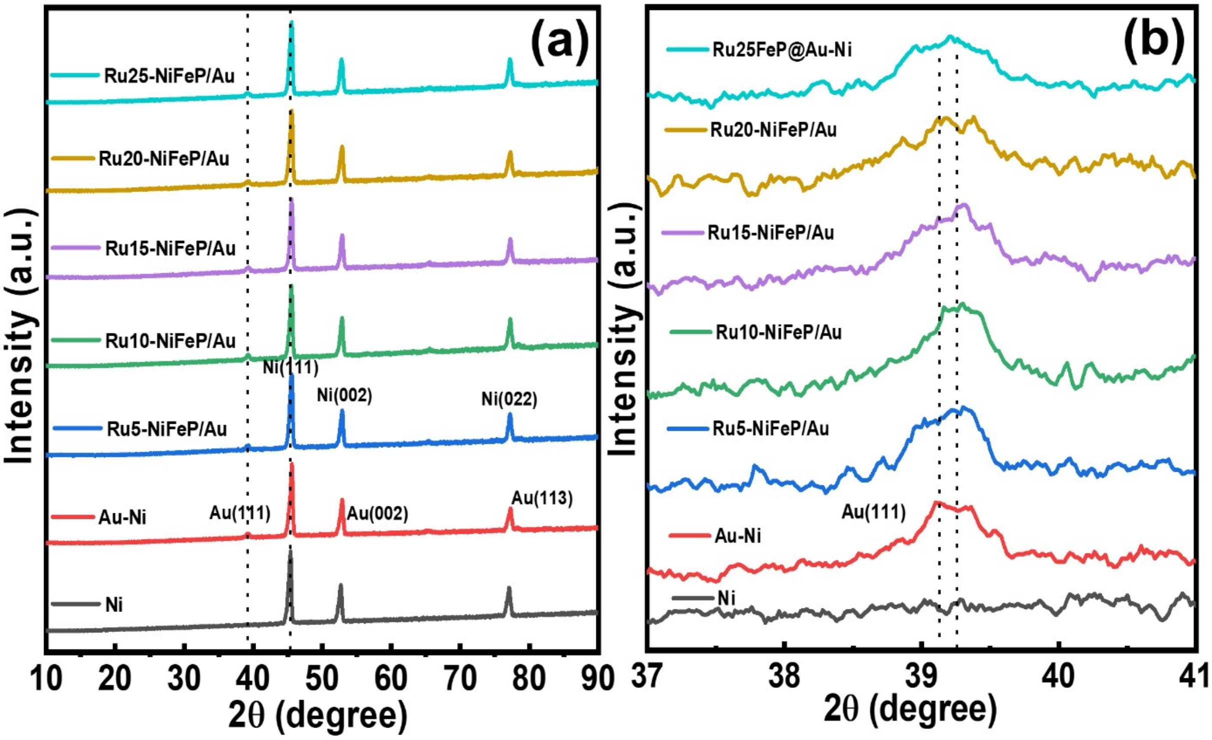

Figure S1. (a) XRD pattern of NF, Au/NF, and RuFeP/NF catalysts. (**b)** Enlarged view of the XRD pattern demonstrating the peak shifts in RuFeP catalysts.

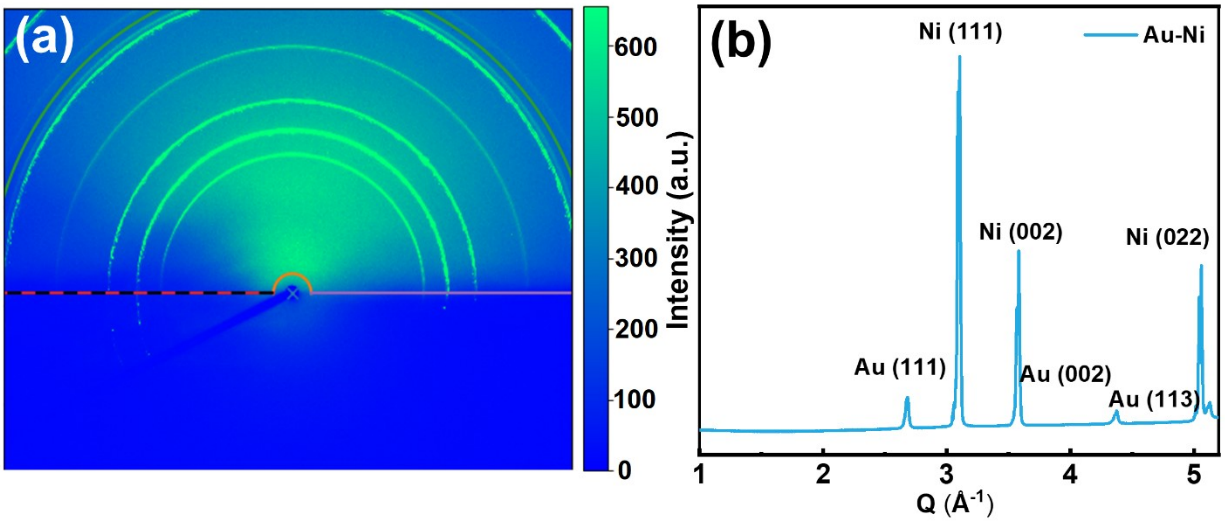

Figure S2. (a) Synchrotron based grazing incident wide X-ray scattering (GI-WAXS) 2D scan image and **(b)** corresponding Q values respectively showing the metallic peaks of Ni and Au. respectively.

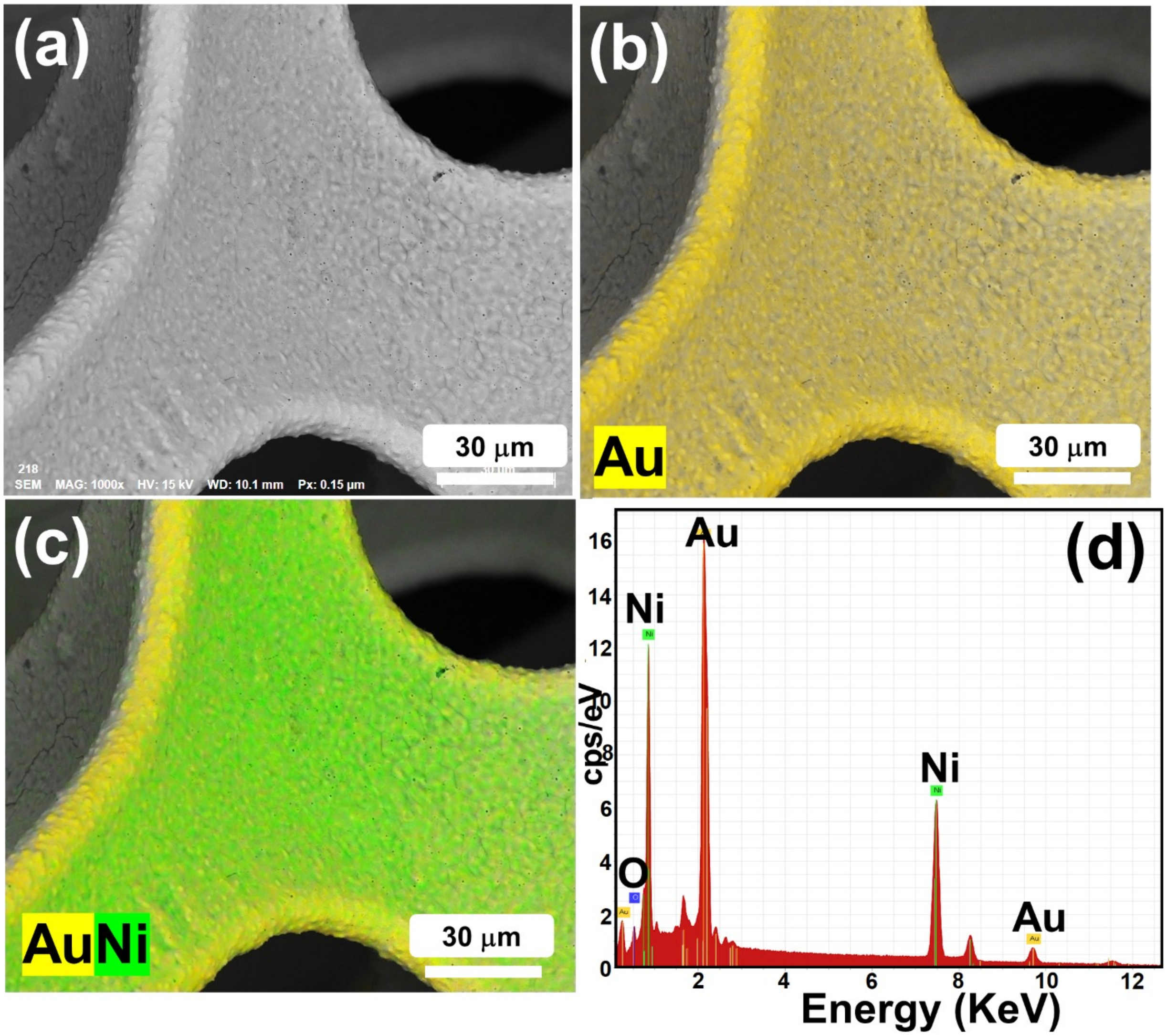

Figure S3. **(a)** Au-NF SEM image, (**b-c)** EDS elemental mapping results of Au and AuNi composite respectively, **(d)** corresponding EDS spectra.

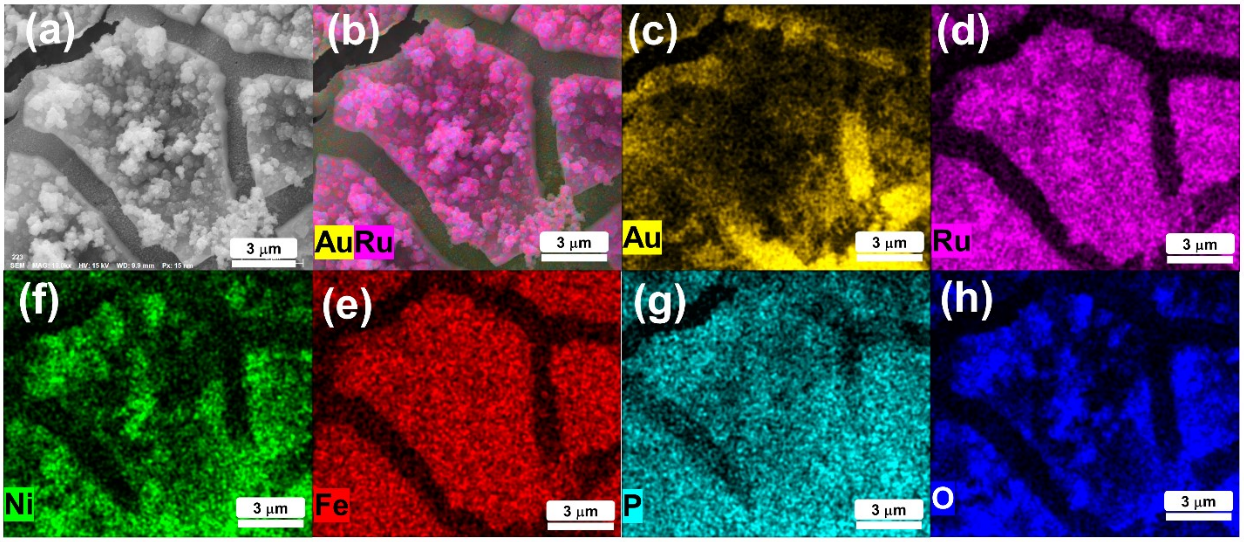

Figure S4. SEM images of Ru5-NiFeP/Au, (**a**) SEM image showing islands of RuFeP, and (**b-h)** elemental mapping for mix composite, Au, Ru, Ni, Fe, P, and O respectively.

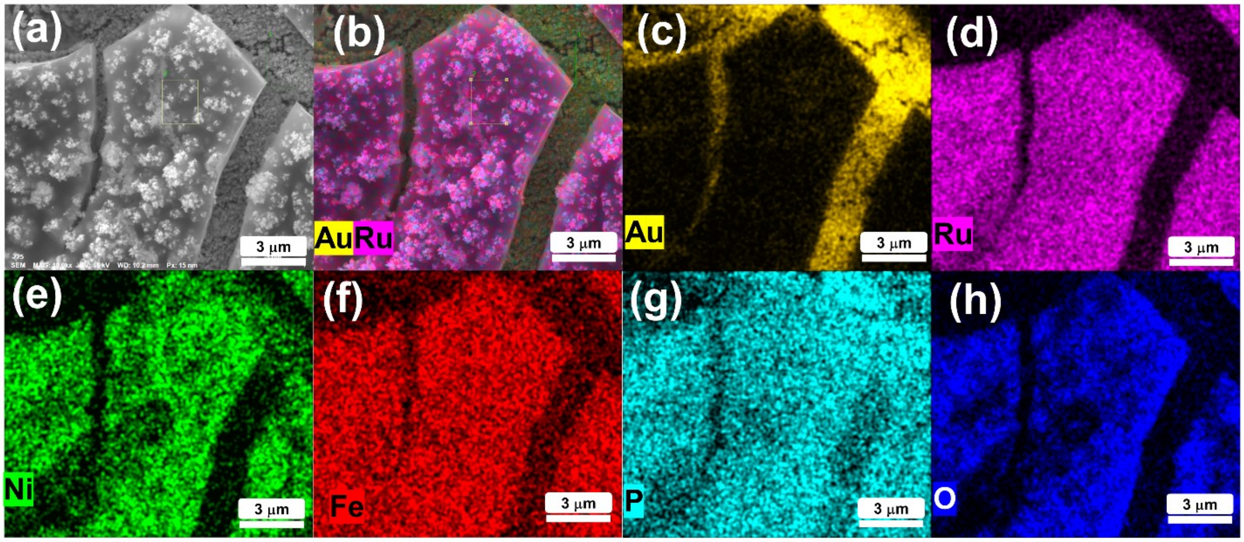

Figure S5. SEM images of Ru10-NiFeP/Au, **(a)** SEM image showing islands of RuFeP, and **(b-h)** elemental mapping for mix composite, Au, Ru, Fe, P, and O respectively.

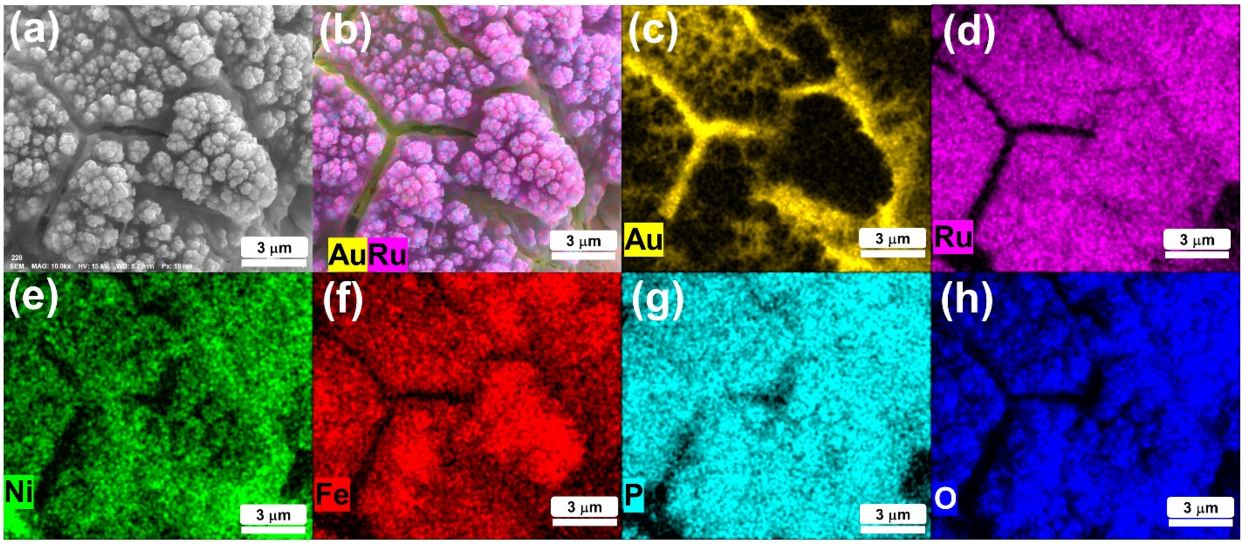

Figure S6. SEM images of Ru15-NiFeP/Au, **(a)** SEM image showing islands of RuFeP, and **(b-g)** elemental mapping for mix composite, Au, Ru, Fe, P, and O respectively.

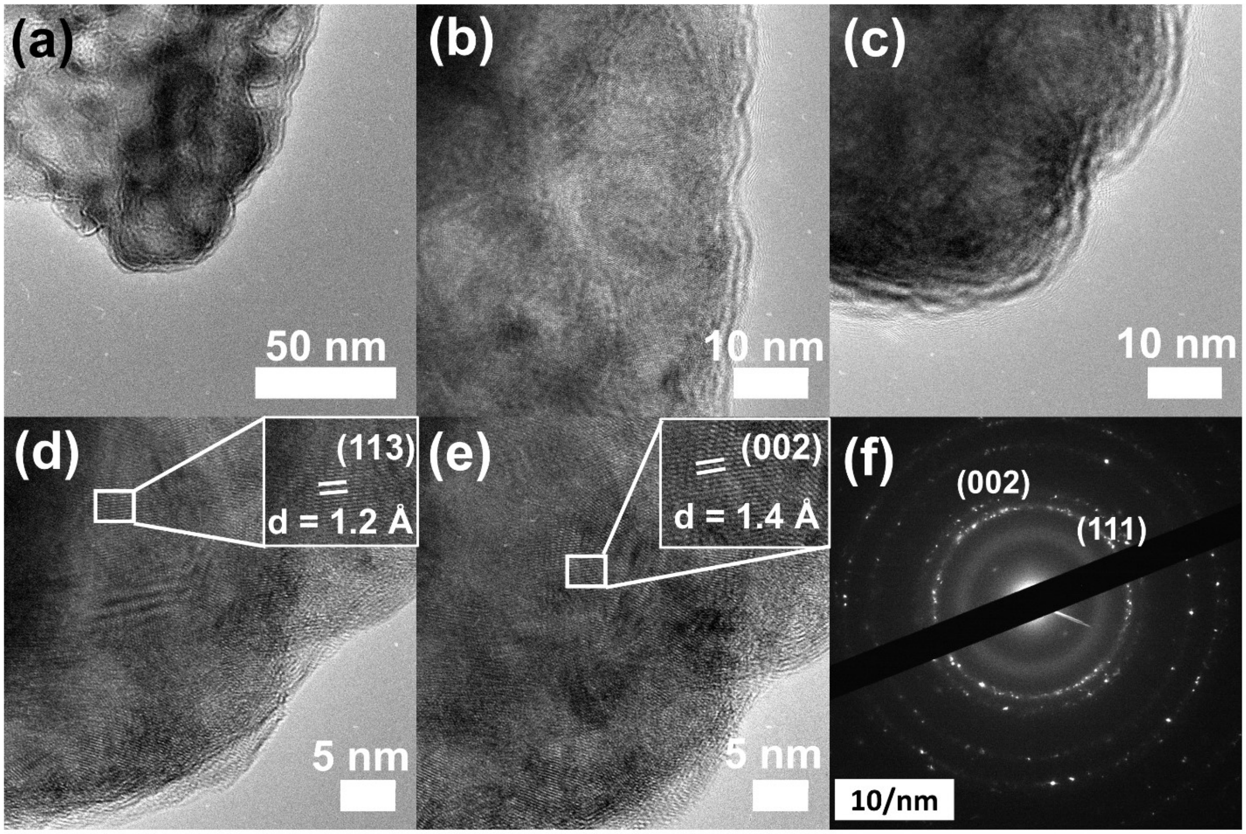

Figure S7. HR-TEM images of Au-Ni and **(a-e)** are the low to high magnification images revealing the layers of Au over Ni and **(f)** is the corresponding SAED pattern showing polycrystalline nature.

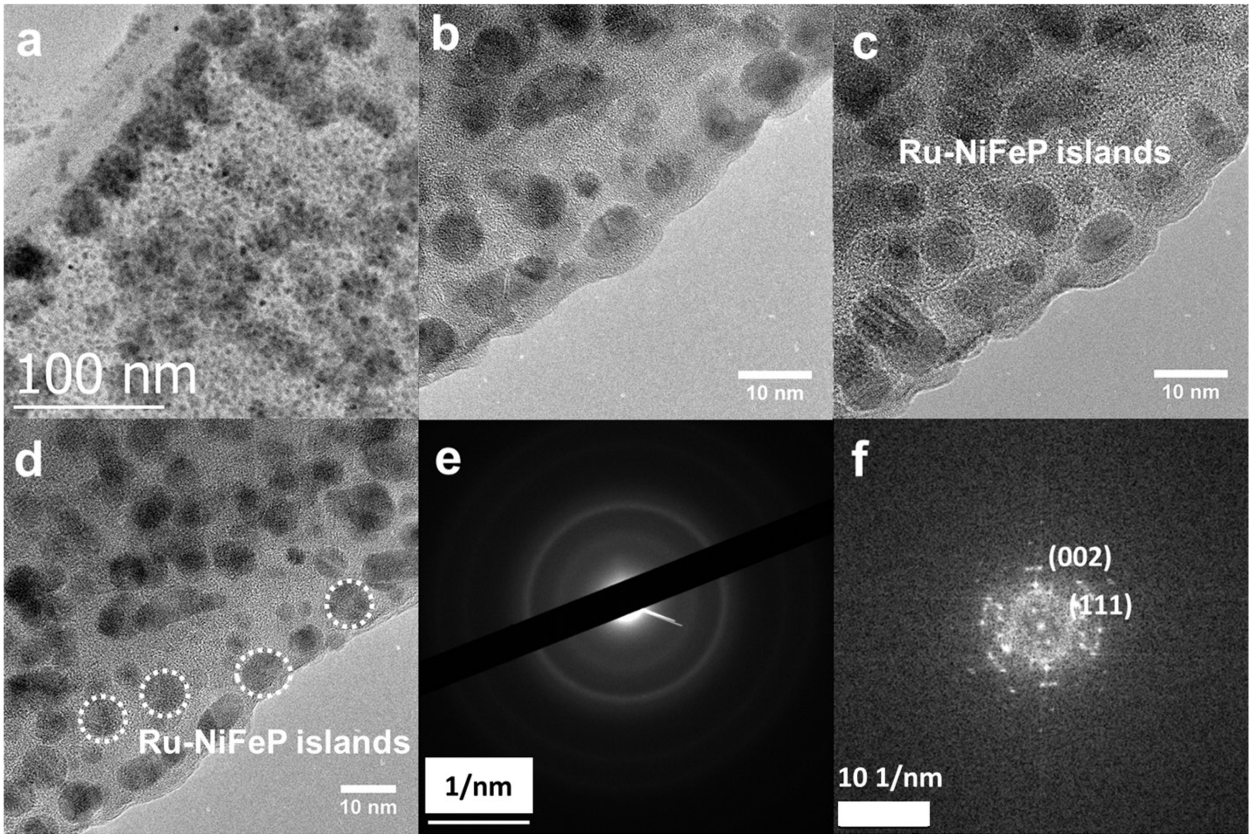

Figure S8. HR-TEM images of Ru15-NiFeP/Au-NF **(a-d)** low to high magnification images showing the island structures and **(e-f)** corresponding SAED pattern displaying amorphous nature and FFT pattern showing polycrystalline nature of Au-Ni.

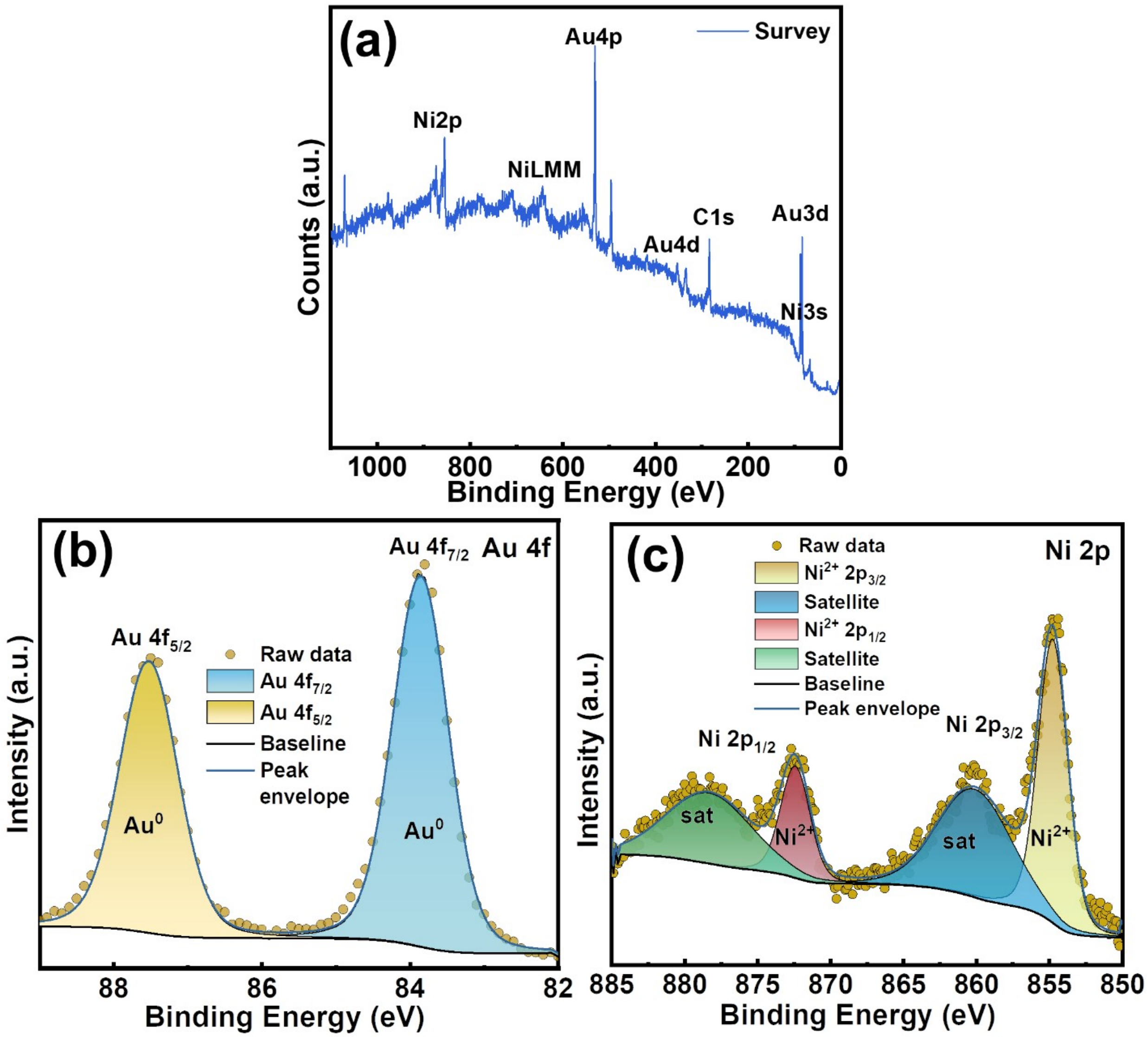

Figure S9. (a) XPS survey scan and HR-XPS spectra of Ru15-NiFeP/Au-NF in **(a)** Au 4f and **(b)** Ni 2p regions respectively.

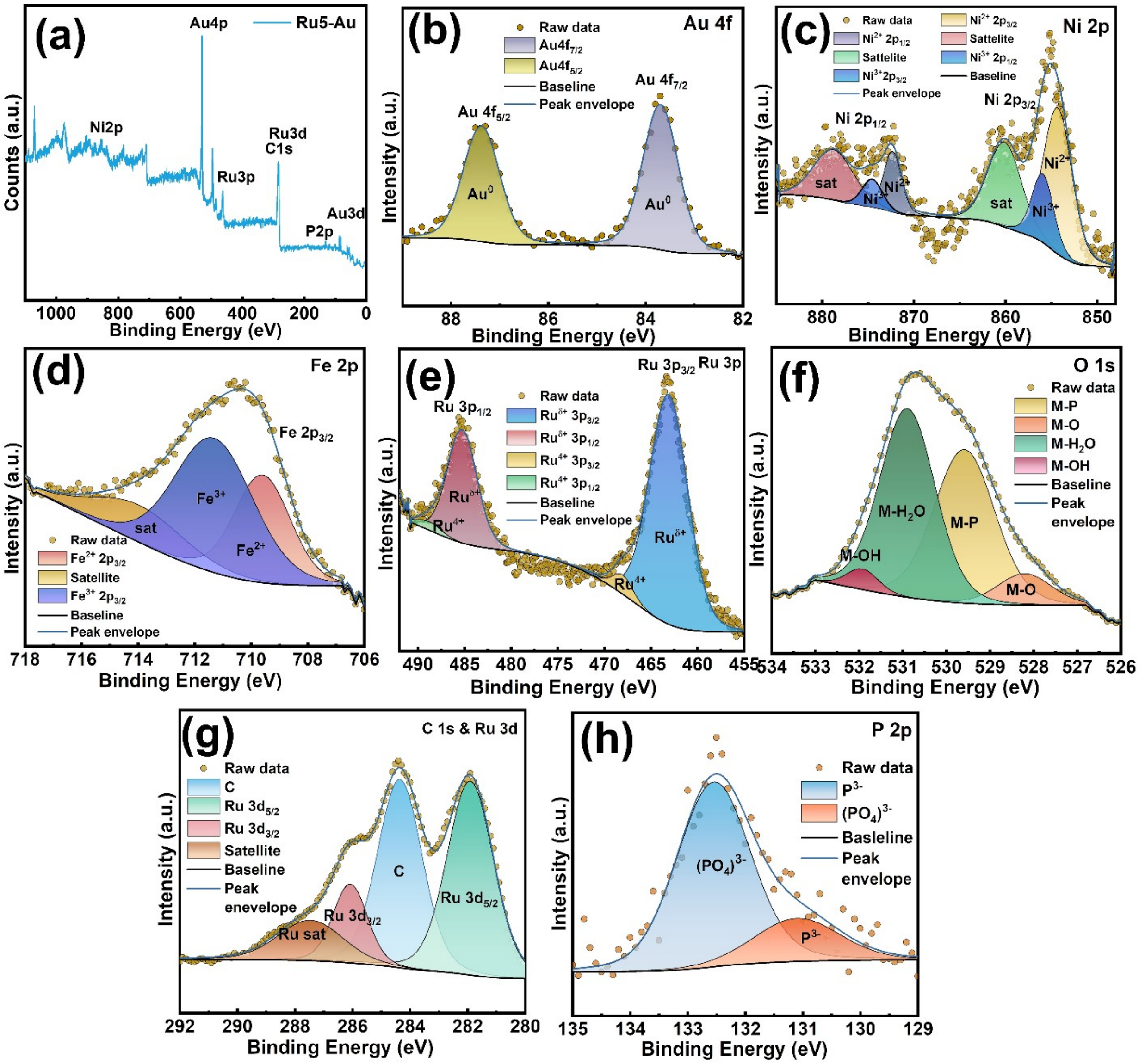

Figure S10. (a) XPS survey scan and **(b-h)** high resolution XPS spectra of Ru5-Au 4f, Ni 2p, Ru 3p, Fe 2p, P 2p, and C1s, Ru3d, and O1s respectively.

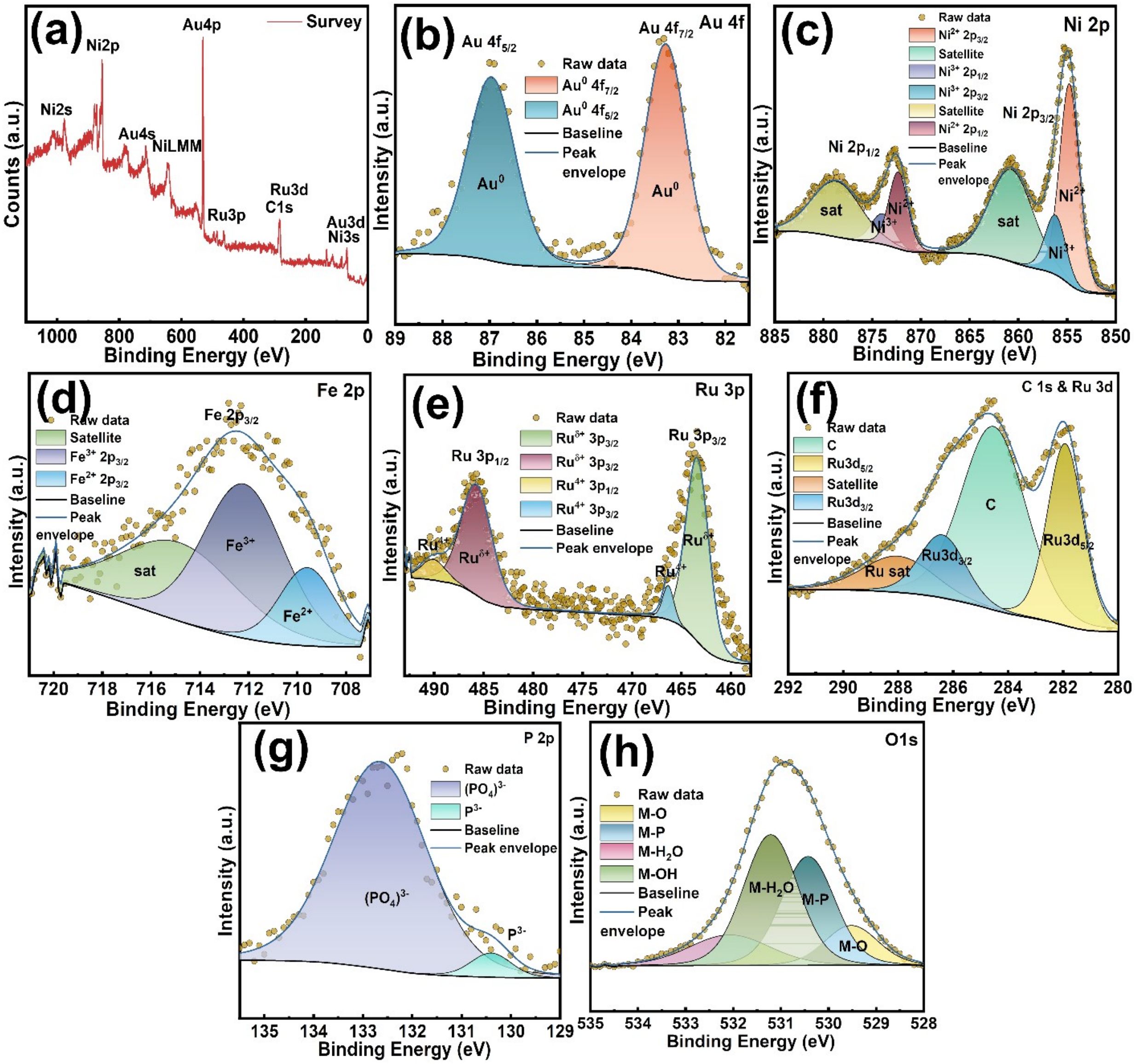

Figure S11. (a) XPS survey scan and **(b-h)** high resolution XPS spectra of Ru15-NiFeP/Au, consisting of Au 4f, Ni 2p, Ru 3p, Fe 2p, P 2p, and C1s, Ru3d, and O1s respectively.

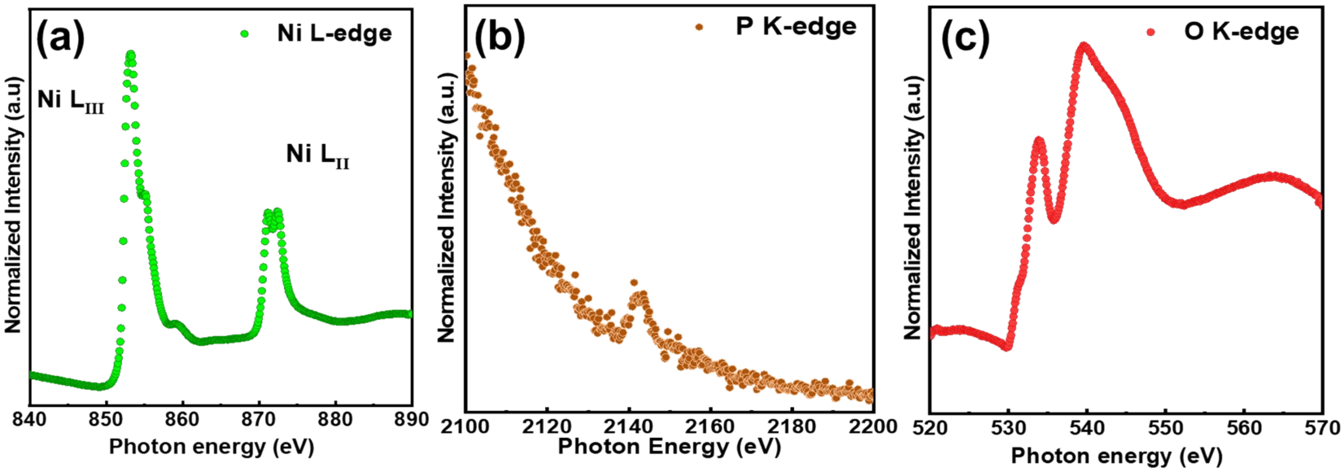

Figure S12. Synchrotron based soft X-ray absorption spectra of Ru15-NiFeP@Au islands. **(a-c)** EEMS scanning profiles of Ni, L, and O respectively.

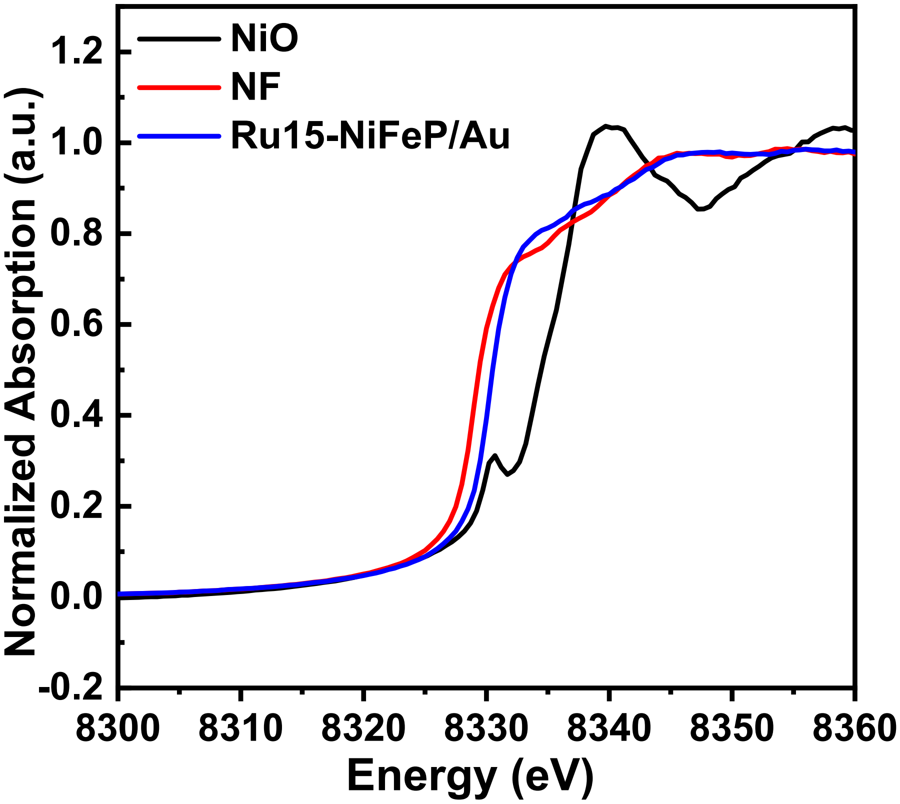

Figure S13. Synchrotron based hard X-ray absorption spectra of Ni-K edge XANES spectra.

Table S1. EXAFS fitting results of Ru15-NiFeP/Au

Atom	Bond	Bond length	CN	ΔE	σ2 (10-3)	R-factor
Fe	Fe-O	1.90 (±0.02)	4.4 (±0.6)	9.2 (±0.9)	9.4 (±0.7)	0.008
	Fe-P	2.34 (±0.05)	4.5 (±0.4)	3.9 (±0.5)	8.8 (±0.9)	
Ru	Ru-O	1.92 (±0.08)	1.3 (±0.3)	6.5 (±0.7)	5.7 (±0.3)	0.008
	Ru-O/P	2.03 (±0.06)	4.6 (±0.5)	3.8 (±0.5)	3.6 (±0.5)	
	Ru-Fe	2.59 (±0.05)	6.9 (±0.8)	0.9 (±0.3)	3.7 (±0.3)	

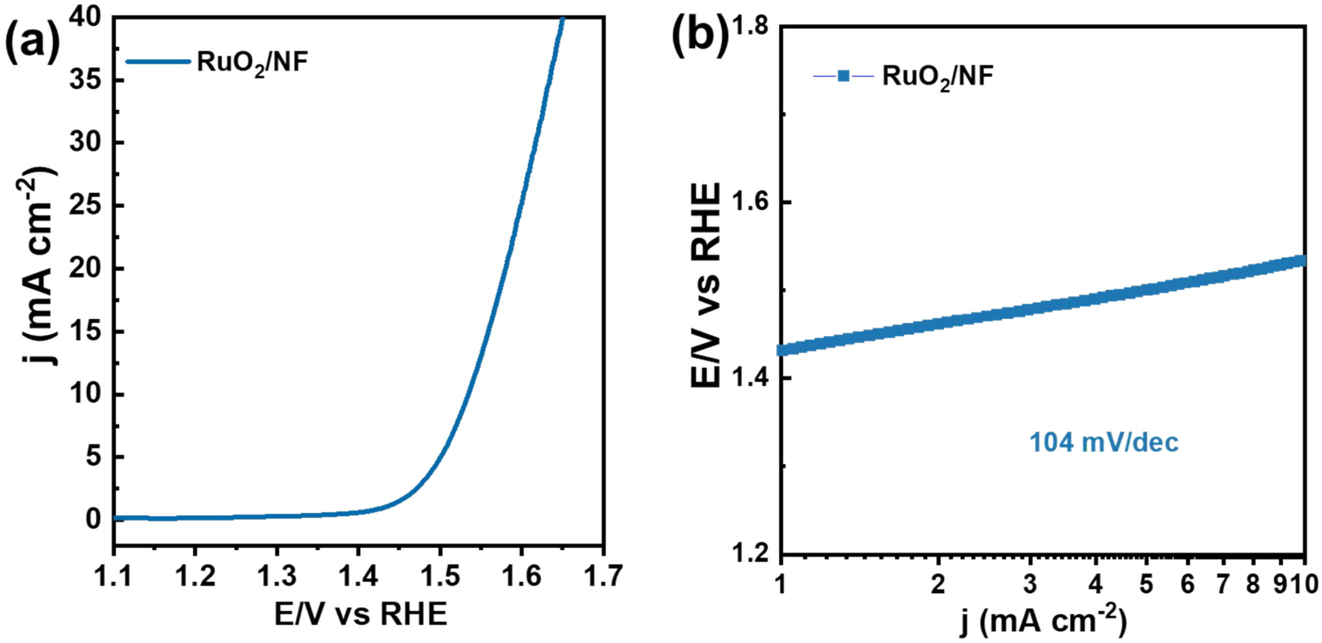

Figure S14. (a) LSV studies of RuO_2/NF and **(b)** Tafel slope in 1 M KOH electrolyte.

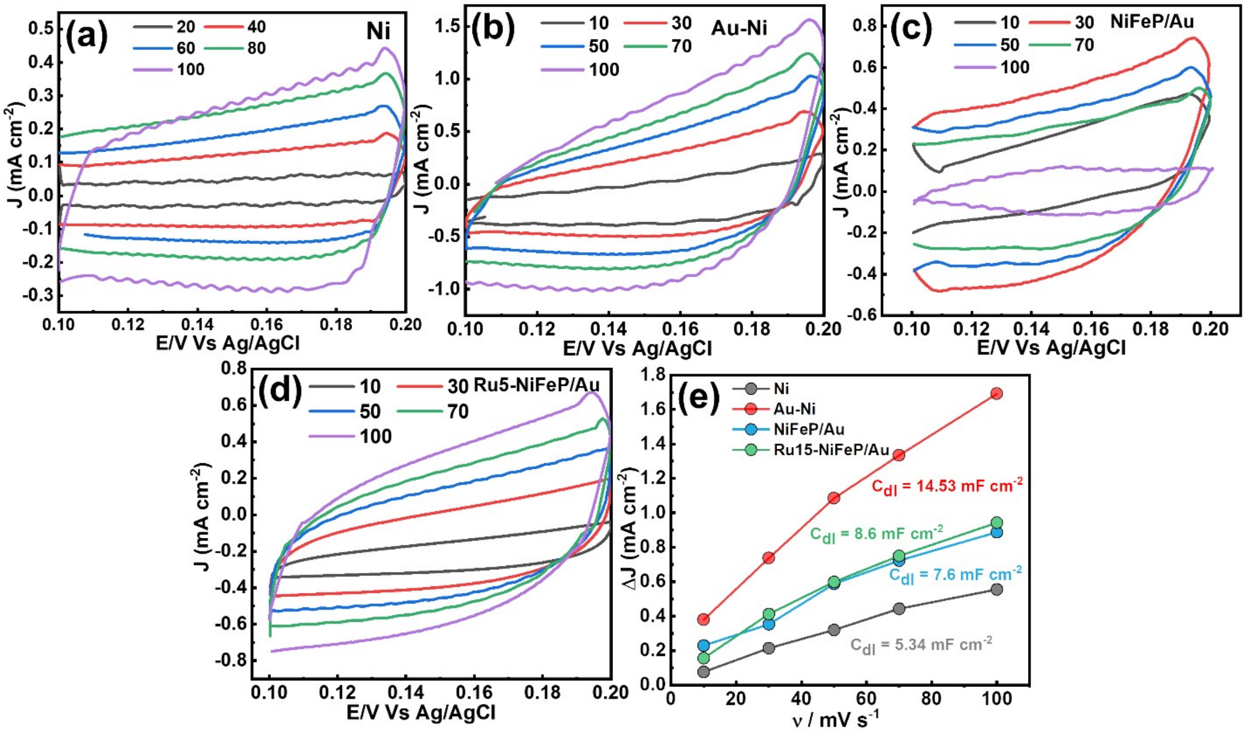

Figure S15. (a-d) Double layer capacitance (C_{dl}) results of Ni, Au-Ni, NiFeP/Au, and Ru5-NiFeP/Au electrodes in non-Faradaic region and **(e)** Plot of Δj vs ν displaying the C_{dl} of each catalyst.

Table S2. Comparison of OER results of Ru15-NiFeP/Au with the literature reports

S. No	Catalyst	Electrolyte	Overpotential (mV) / mA cm^{-2}	References
1	3DG−Au-Ni_3S_2	1 M KOH	370 mV @ 91 mA cm^{-2}	[1]
2	Au/$NiCo_2O_4$	1 M KOH	360 mV @ 10 mA cm^{-2}	[2]
3	Ni/Au/Cysteine	0.1 M KOH	310 mV @ 10 mA cm^{-2}	[3]
4	$Fe_{0.14}Co_{0.86}$-P/CC	1 M KOH	270 mV @ 10 mA cm^{-2}	[4]
5	Co_2P/FeP-FeP_4	1 M KOH	230 mV @ 10 mA cm^{-2}	[5]
6	CoP/FeP/CeOx	1 M KOH	285 mV @ 10 mA cm^{-2}	[6]
7	CoP/FeP/CP	1 M KOH	260 mV @ 10 mA cm^{-2}	[7]
8	CoP/FeP	1 M KOH	280 mV @ 10 mA cm^{-2}	[8]
9	RuP/NPC	1 M KOH	310 mV @ 10 mA cm^{-2}	[9]
10	NiFeP@NiP@NF	1 M KOH	227 mV @ 10 mA cm^{-2}	[10]
11	Co-NiP@NC	1 M KOH	280 mV @ 10 mA cm^{-2}	[11]
12	Ni_2P/C-500	0.1 M KOH	260 mV @ 10 mA cm^{-2}	[12]
13	$Ni(PO_3)_2$	1 M KOH	342 mV @ 10 mA cm^{-2}	[13]
14	Ni_2P/FeP_4/CoP	1 M KOH	274 mV @ 10 mA cm^{-2}	[14]
15	NiFeP/Zn	1 M NaOH	262 mV @ 10 mA cm^{-2}	[15]
16	NiFeP-rGO	1 M KOH	250 mV @ 10 mA cm^{-2}	[16]
17	NiFeP-MOF	1 M KOH	274 mV @ 10 mA cm^{-2}	[17]
18	CrNiFeP/NC	1 M KOH	249 mV @ 10 mA cm^{-2}	[18]
19	*Ru15-NiFeP/Au*	*1 M KOH*	*223 mV @ 10 mA* cm^{-2}	*This work*

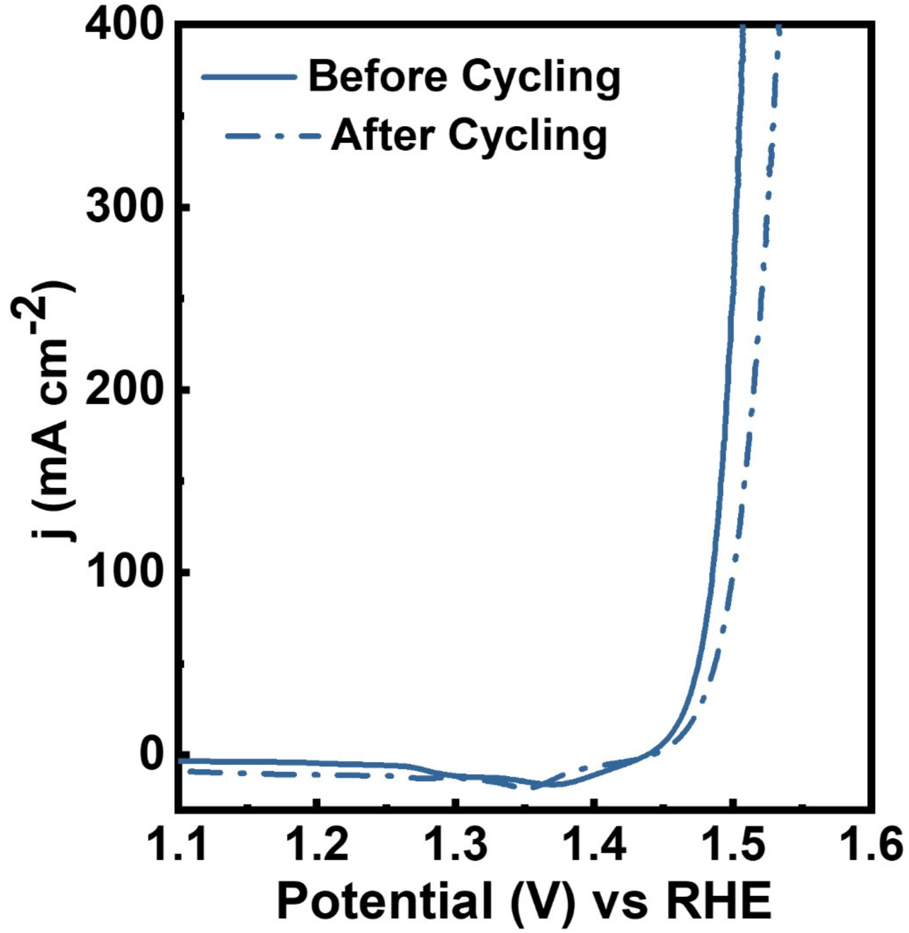

Figure S16. LSV before and after the OER cycling study for 500 cycles at 200 mV/sec scan rate for Ru15-NiFeP/Au electrode in 1M KOH.

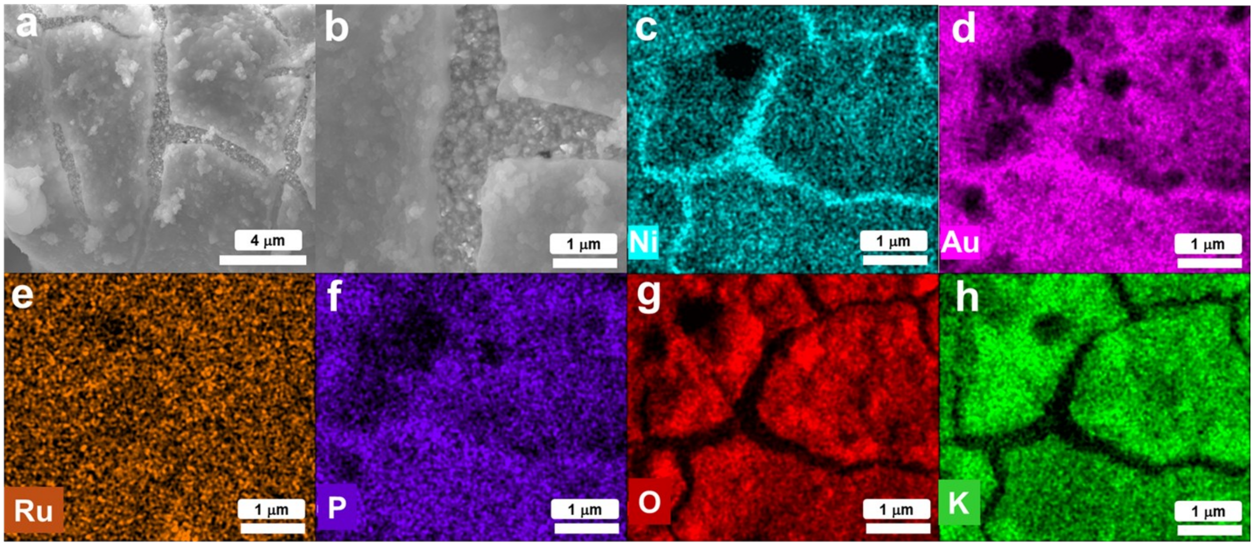

Figure S17. Post OER SEM images of Ru15-NiFeP/Au. (a and b) are the RuNiFeP islands similar to before OER studies and (c-h) are the color mapping results of Ni, Au, Ru, P, O and K respectively and here K arises from the electrolyte KOH used.

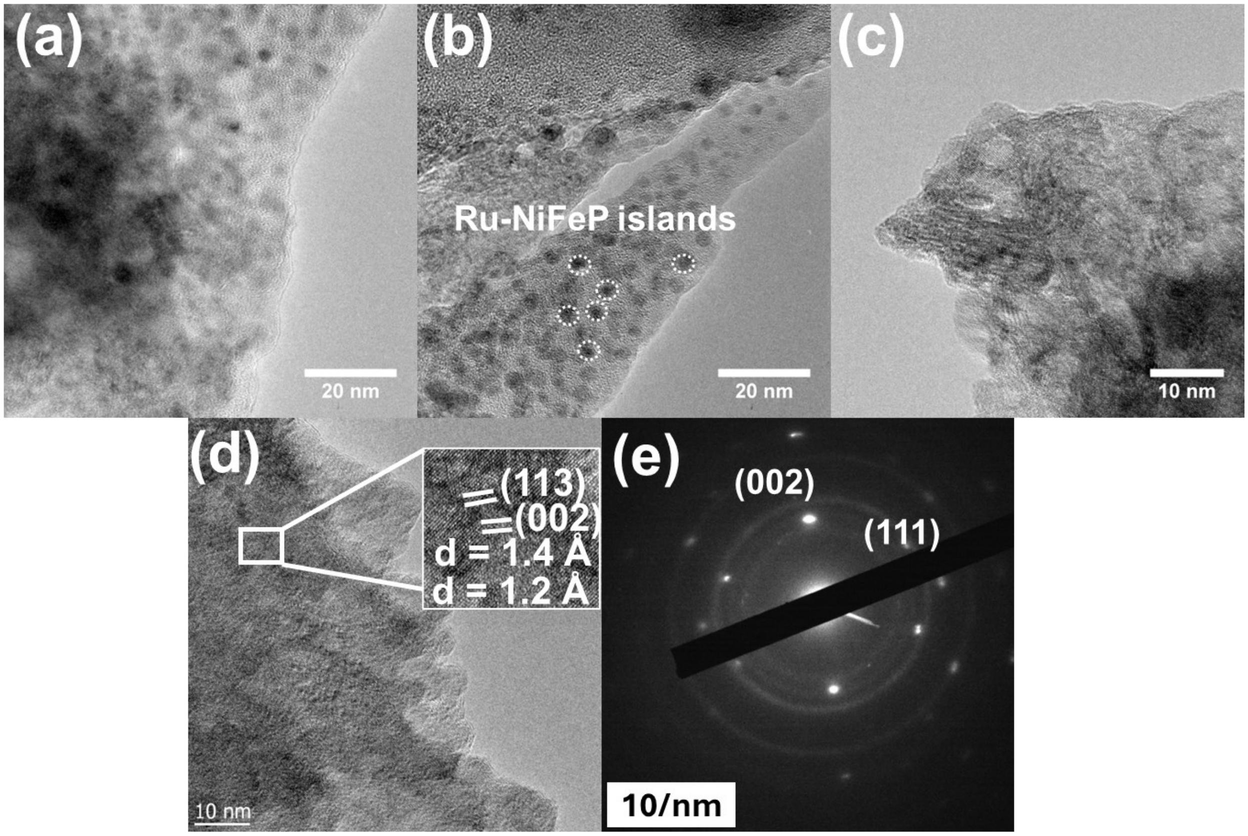

Figure S18. Post OER HR-TEM images of Ru15-NiFeP/Au. **(a-c)** High magnified images showing the islands of Ru15-NiFeP similar to that of before OER. **(d)** High magnification image and the inset shows the lattice fringes and (f) corresponding SAED pattern.

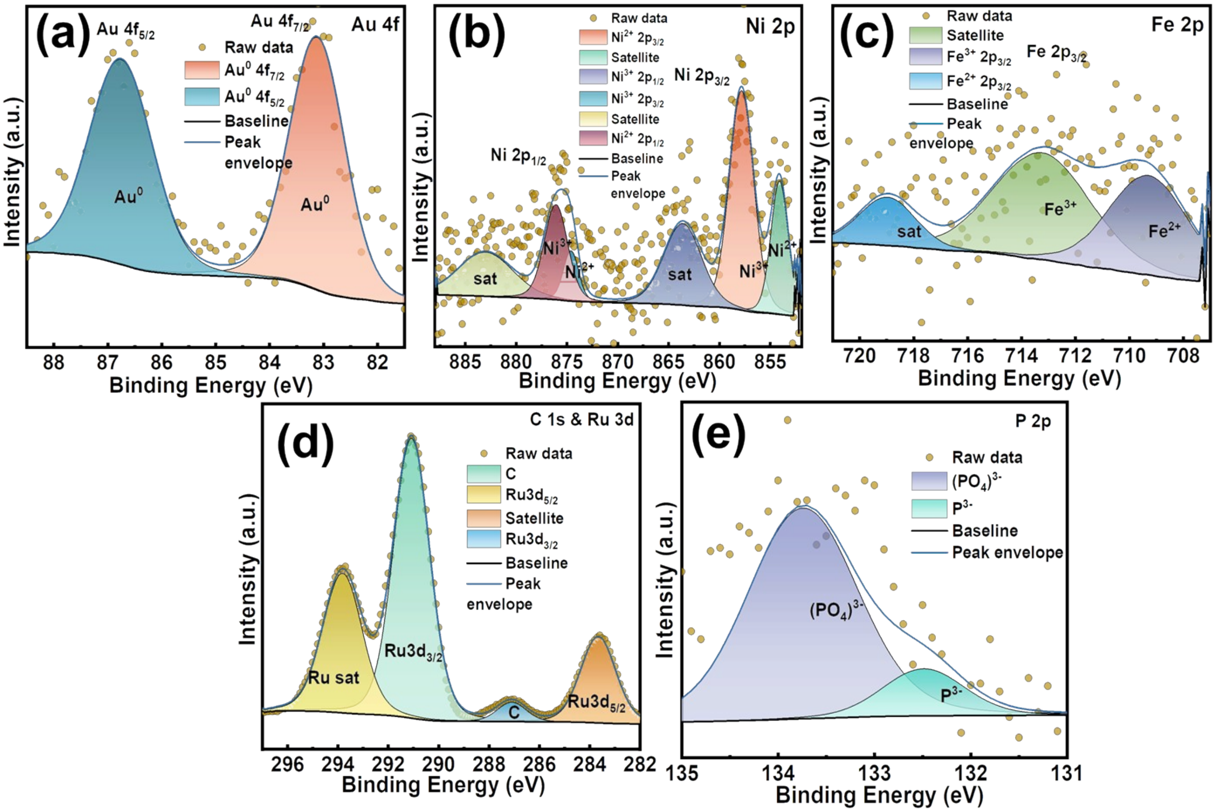

Figure S19. Post OER HR-XPS spectra of Ru15-NiFeP/Au-NF in **(a-e)** High resolution spectra of Au 4f, Ni 2p, Fe 2p, C1s, Ru3d, and P 2p respectively.

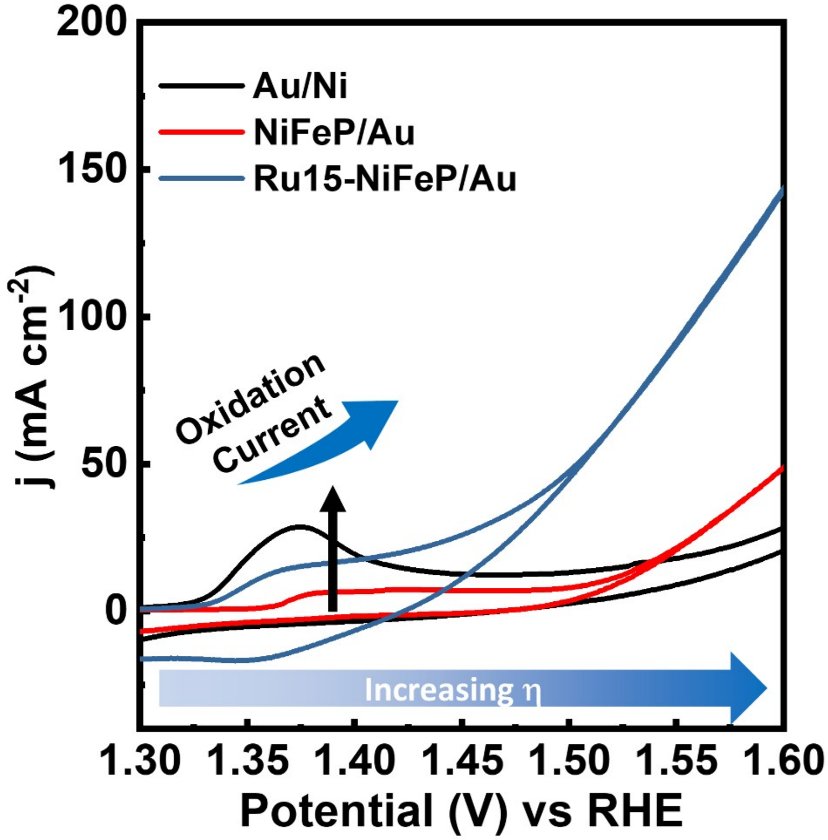

Figure S20. iR uncorrected CV from 1.3 to 1.6 V vs RHE chosen for studying electrode/electrolyte interface by *in-situ* EIS studies.

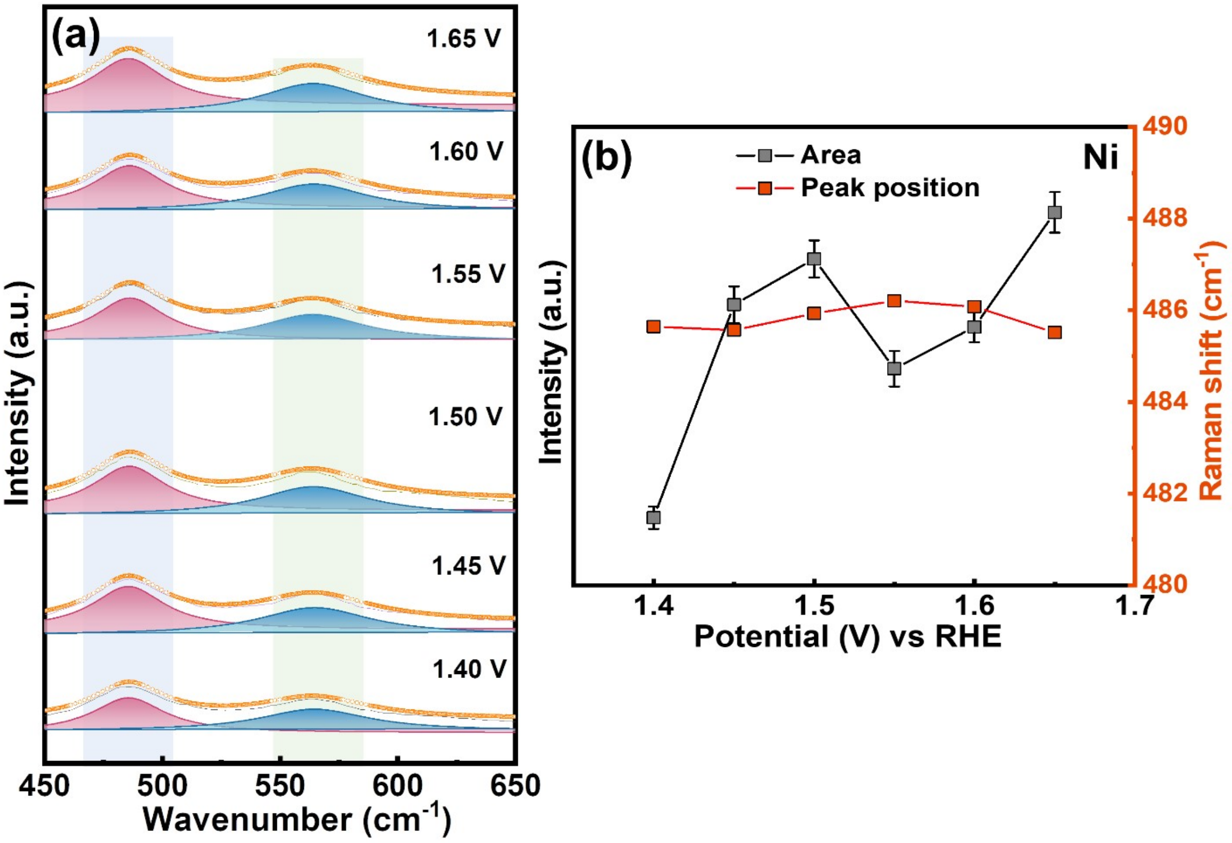

Figure S21. (a) *In-situ* SERS studies of bare NF and **(b)** Fitted peak area for NiOOH and the corresponding intensities.

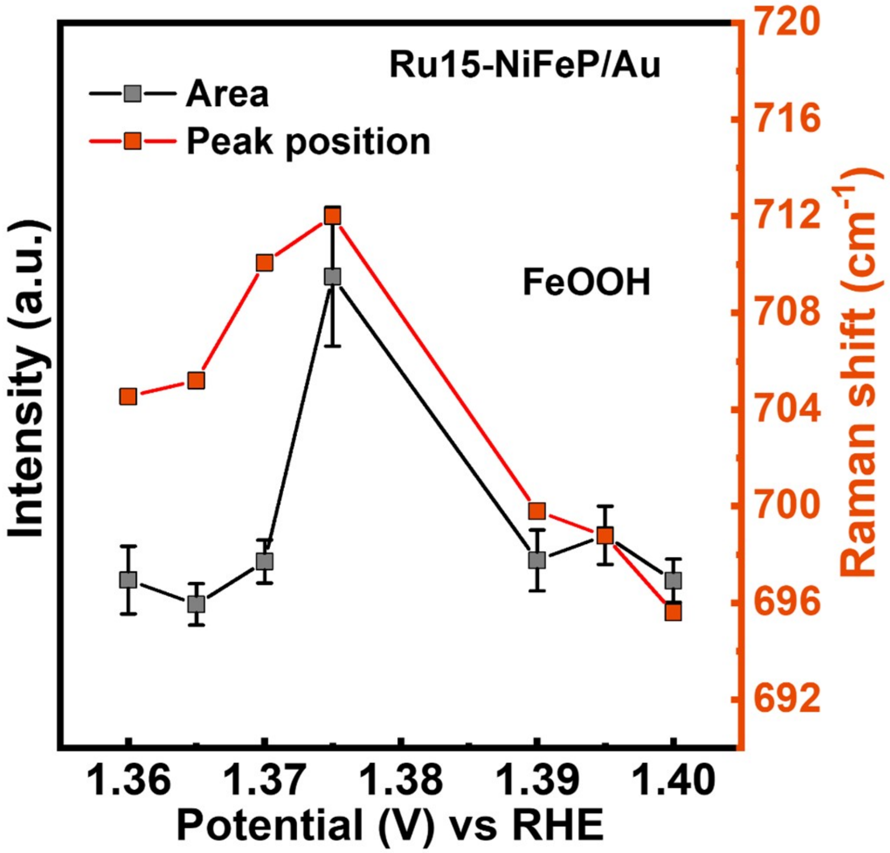

Figure S22. *In-situ* SERS studies of Ru15-NiFeP/Au showing the fitted peak area and intensities of FeOOH.

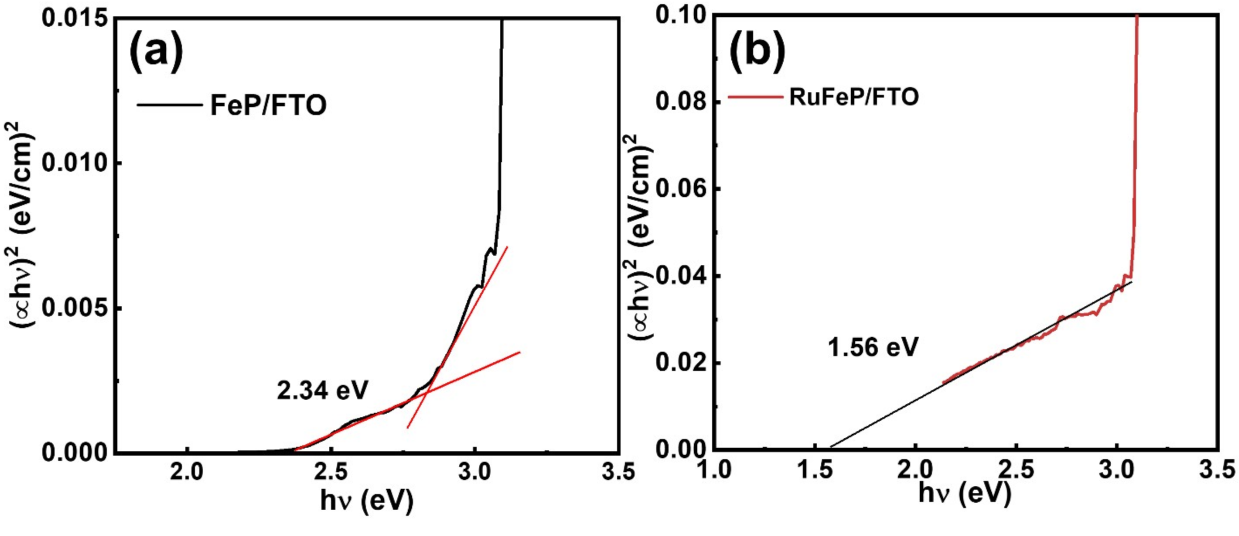

Figure S23. (a) Tauc plot of FeP and **(b)** Tauc plot of RuFeP demonstrating the role of Ru in the reduction of band gap.

2.Density Functional Theory (DFT) study

2.1. Computational Methodology

To gain atomistic insights into the oxygen evolution reaction mechanism on RuO over NiFeOOH system, first-principles calculations were performed using density functional theory as implemented in Vienna ab-initio simulation (VASP 6.2.0) package.[19] The electron exchange and correlations were approximated using Perdew-Burke-Ernzerhof (PBE) generalized gradient approximation (GGA).[20] The electron-ion interactions were described by all electron projector augmented wave (PAW) pseudopotentials.[21] The dispersion energy corrections were incorporated using DFT+D3 approach of Grimme et al.[22] A supercell of size 2*2*1 was constructed to explore the maximum surface sites with non-equivalent chemical environment. The periodic images were separated by a vacuum of 20 Å along z direction to prevent spurious interactions. The Brillouin zone was sampled using 2*4*1 Monkhorst-Pack k-grid, for all structures. The optimization of all structures was performed using a conjugate gradient scheme until the convergence criteria for energies and the forces reached 10^{-5} eV and 0.01 eV $Å^{-1}$, respectively. The strong correlation effects of d-electrons for Fe and Ni were accounted using DFT+U method with U_{eff}= 2.5 eV, 4.8 eV and 4.0 eV for Fe, Ni and Ru, respectively. Bader charge scheme, as implemented in Henkelman code,[23] was utilized to study the degree of charge distribution.

Ideally, OER is a $4e^-$ transfer process, consisting of four intermediate steps.[24] The mechanism of oxygen reduction reaction is as follows:

$$* + H_2O \rightarrow *OH + H^+ + e^- \quad (1)$$

$$*OH \rightarrow *O + H^+ + e^- \quad (2)$$

$$*O + H_2O \rightarrow *OOH + H^+ + e^- \quad (3)$$

$$*OOH \rightarrow * + O_2 + H^+ + e^- \quad (4)$$

where * represent the catalytic surface.

The overpotential of OER process depends on the adsorption of intermediates on the catalytic surface. Hence, *OOH, *OH and *O intermediates are first adsorbed on NiFe-OOH at type-1 and type-2 surface sites and, on the type-1 and type-2 RuO/NiFe-OOH at Ru, Then, the adsorption energy of intermediates involved are calculated using the following equations:

$$\Delta E_{ads}(OH) = E(^*OH) - [E^* + E(H_2O) - 0.5E(H_2)] \tag{1}$$

$$\Delta E_{ads}(O) = E(^*O) - [E^* + E(H_2O) - E(H_2)] \tag{2}$$

$$\Delta E_{ads}(OOH) = E(^*OOH) - [E^* + 2E(H_2O) - 1.5E(H_2)] \tag{3}$$

$\Delta E_{ads}(OH)$, $\Delta E_{ads}(O)$ and $\Delta E_{ads}(OOH)$ are the adsorption energies of *OH, *O and *OOH intermediates, respectively. $E(^*OH)$, $E(^*O)$ and $E(^*OOH)$ are the total energy of the system (surface + intermediate), E^* is the energy of the surface, $E(H_2O)$ and $E(H_2)$ are the energy of the reference molecules. To further analyze the thermodynamics of the reaction, the calculated adsorption energies were used to obtain the Gibbs free energies using the following equation[24]:

$$\Delta G = \Delta E_{ads} + \Delta ZPE - T\Delta S + \Delta G_U \tag{4}$$

The Gibbs free energy for OER reaction is given as [6]:

$$\Delta G = \Delta E_{ads} + \Delta ZPE - T\Delta S - eU \tag{5}$$

Here, ΔZPE is the difference in zero-point energies of the species, and *e* represents number of electrons transferred. Only vibrational energy contribution was considered during the calculation of entropies (**Table S5-S8**). The zero-point energy calculations were performed using vaspkit.[25] ΔG_U represents the free energy correction due to electrode potentials. The temperature was taken to be 298.18 K.

Gibbs free energy for all the steps (Eq 1-4) are ΔG_1, ΔG_2, ΔG_3 and ΔG_4, respectively. The potential limiting step is given as,

$$\Delta G_{PLS} = \max \{\Delta G_1, \Delta G_2, \Delta G_3, \Delta G_4\} \tag{6}$$

The limiting potential,

$$U_L = -\frac{\Delta G_{PLS}}{e}$$

The theoretical overpotential is given as

$$\eta_{OER} = U_L - 1.23 \text{ V} \tag{7}$$

where 1.23V is the theoretical potential for water splitting.

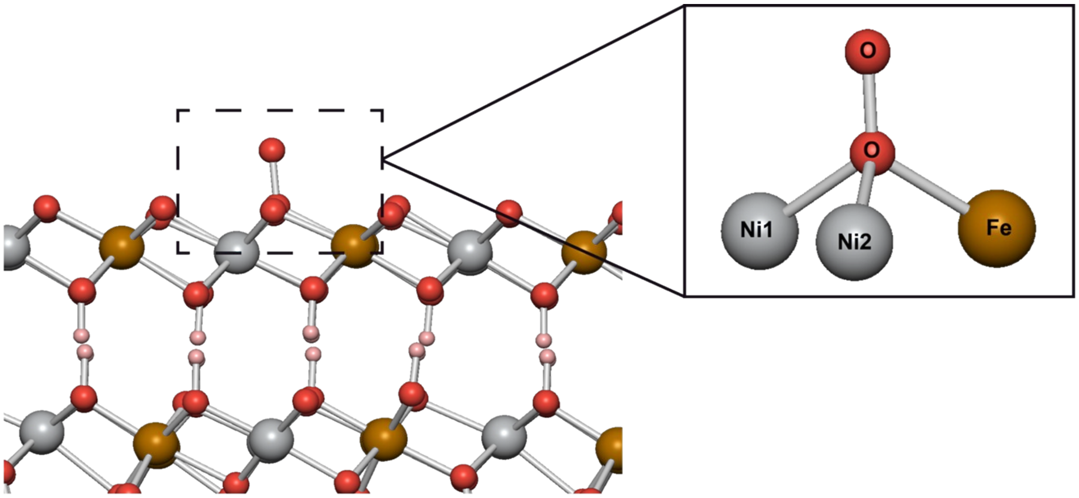

Figure S24. DFT study demonstrating the structure of O intermediate on type-1 NiFe-OOH.

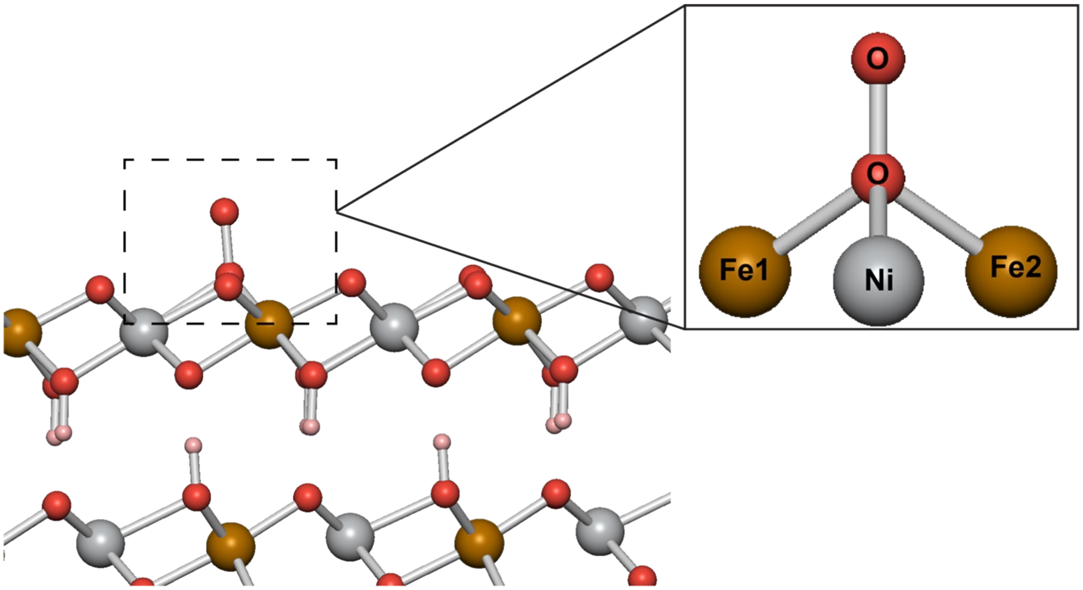

Figure S25. DFT study demonstrating the structure of O intermediate on type-2 NiFe-OOH.

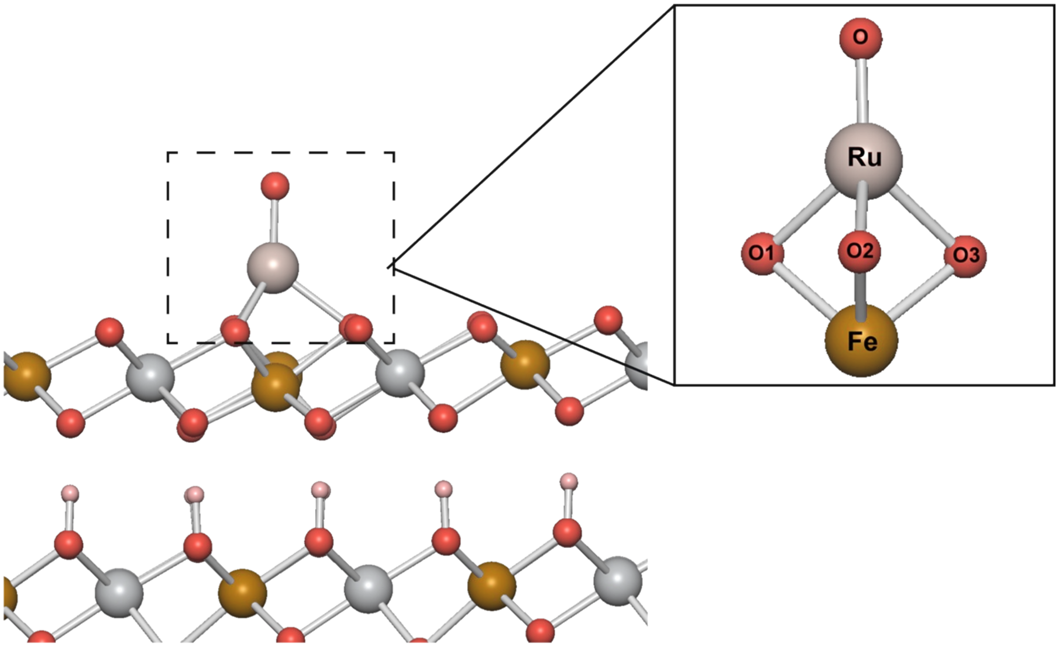

Figure S26. DFT study demonstrating the structure of O intermediate on type-1 Ru-O/NiFe-OOH.

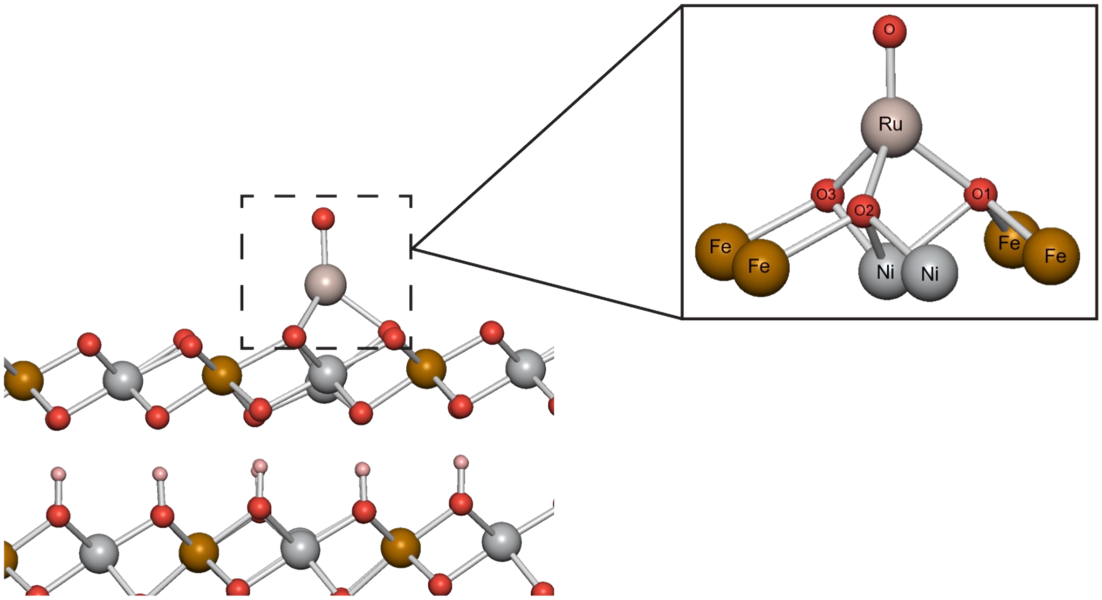

Figure S27. DFT study demonstrating the structure of O intermediate on type-2 Ru-O/NiFe-OOH.

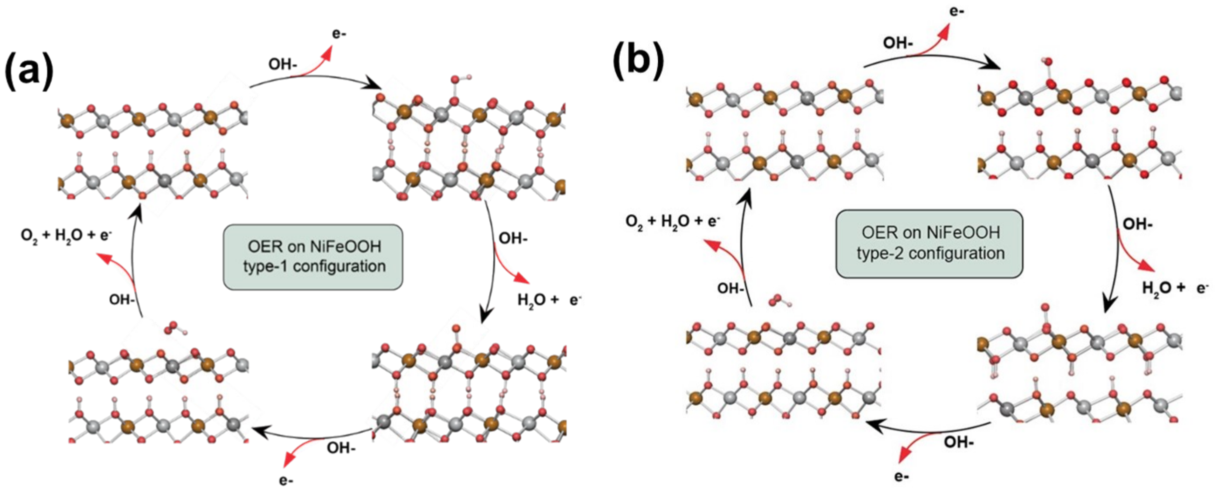

Figure S28. OER pathways in, **(a)** type-1 NiFe-OOH **(b)** type-2 NiFe-OOH.

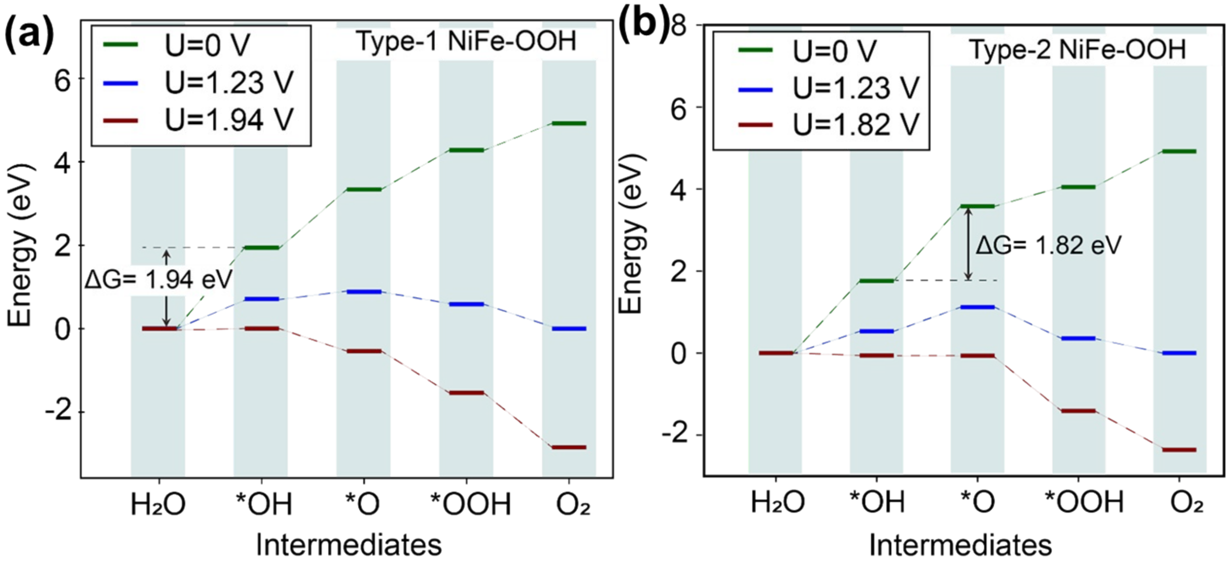

Figure S29. (a-b) OER Free energy diagram of **(a)** type-1 NiFe-OOH **(b)** type-2 NiFe-OOH.

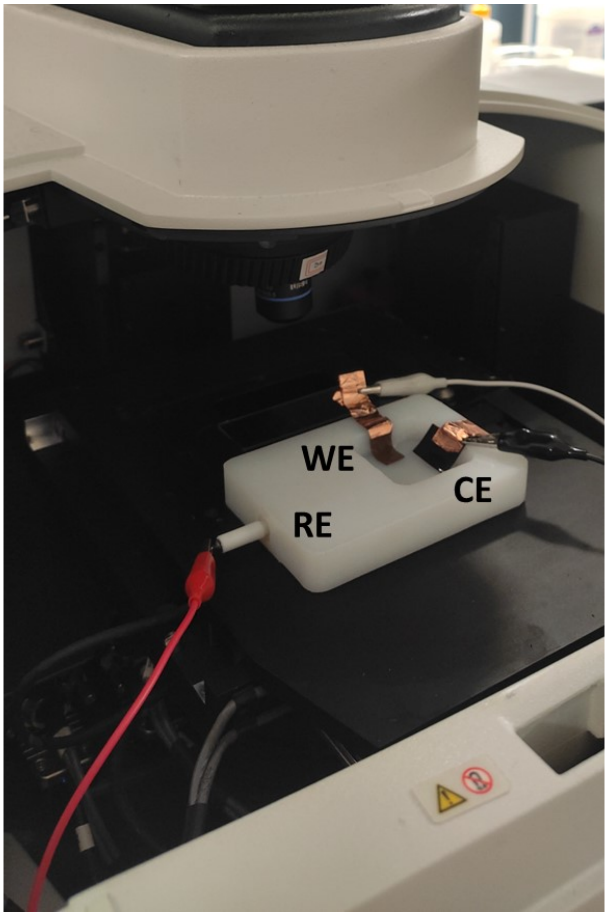

Figure S30. Custom made in-situ SERS cell setup with Ru15-NiFeP/Au working electrode, Carbon cloth counter electrode and Ag/AgCl reference electrode respectively.

Bader Charge Analysis

Table S3. Bader charge analysis for type-1 NiFe-OOH configuration

S.No.	Type-1 NiFe-OOH	O	*O	*O	*H	Ni1	Ni2	Fe
1.	* + OH	-0.44	-0.58	-	0.63	1.30	1.28	1.42
2.	* + O	-0.44	-0.07	-	-	1.29	1.27	1.45
3.	* + OOH	-0.61	-0.02	-0.47	0.69	1.33	1.32	1.47

Table S4. Bader charge analysis for type-2 NiFe-OOH configuration

S.No.	Type-2 NiFe-OOH	O	*O	*O	*H	Ni	Fe1	Fe2
1.	* + OH	-0.49	-0.54	-	0.61	1.34	1.45	1.45
2.	* + O	-0.42	-0.12	-	-	1.25	1.45	1.44
3.	* + OOH	-0.64	-0.03	-0.45	0.65	1.34	1.47	1.47

Table S5. Bader charge analysis for type-1 RuO/NiFe-OOH

S.No.	Type-2 RuO/NiFe-OOH	O	O1	O2	O3	*O	*O	*H	Ru	Ni
1.	Surface (*)	-0.54	-0.90	-0.88	-0.88	-	-	-	1.50	1.21
2.	* + OH	-0.58	-0.87	-0.88	-0.87	-0.98	-	0.57	1.61	1.30
3.	* + O	-0.33	-0.92	-0.86	-0.86	-0.28	-	-	1.51	1.18
4.	* + OOH	-0.58	-0.87	-0.88	-0.87	-0.36	-0.56	0.58	1.61	1.30

Table S6. Bader charge analysis for type-2 RuO/NiFe-OOH

S.No.	Type-1 RuO/NiFe-OOH	O	O1	O2	O3	*O	*O	*H	Ru	Fe
1.	Surface (*)	-0.61	-0.87	-0.91	-0.91	-	-	-	1.52	1.32
2.	* + OH	-0.63	-0.89	-0.93	-	-0.98	-	0.64	1.61	1.43
3.	* + O	-0.54	-0.93	-0.93	-	-0.54	-	-	1.82	1.43
4.	* + OOH	-0.61	-0.88	-0.90	-	-0.36	-0.60	0.64	1.62	1.40

Gibbs Free Energy calculations

Table S7. Gibbs free energy for type-1 NiFe-OOH at U= 0V, 1.23 V and 1.94 V

Type1 NiFeOOH	Adsorption Energy(eV)	Δ(Z-ΔTS)	ΔG(U=0 V)	ΔG(U=1.23 V)	ΔG(U=1.94 V)
OH	2.09	-0.42	1.94	0.71	0.0039
O	3.65	-0.31	3.34	0.88	-0.537
OOH	4.71	-0.44	4.28	0.59	-1.54

Table S8. Gibbs free energy for type-2 NiFe-OOH at U= 0V, 1.23 V and 1.82 V

Type2 NiFeOOH	Adsorption Energy(eV)	Δ(Z-ΔTS)	ΔG(U=0 V)	ΔG(U=1.23 V)	ΔG(U=1.82 V)
OH	1.86	-0.10	1.76	0.53	-0.058
O	3.89	-0.31	3.58	1.12	-0.064
OOH	4.54	-0.49	4.05	0.36	-1.41

Table S9. Gibbs free energy for type-1 RuO/NiFe-OOH at U= 0V, 1.23 V and 1.58 V

Type1 RuO/NiFeOOH	**Adsorption Energy(eV)**	**Δ(Z-ΔTS)**	**ΔG(U=0 V)**	**ΔG(U=1.23 V)**	**ΔG(U=1.58 V)**
OH	1.02	-0.11	0.91	-0.32	-0.67
O	2.32	-0.29	2.03	-0.43	-1.13
OOH	4.07	-0.45	3.61	-0.08	-1.13

Table S10. Gibbs free energy for type-2 RuO/NiFe-OOH at U= 0V, 1.23 V and 1.70 V

Type2 RuO/NiFeOOH	**Adsorption Energy(eV)**	**Δ(Z-ΔTS)**	**ΔG(U=0 V)**	**ΔG(U=1.23 V)**	**ΔG(U=1.70 V)**
OH	0.85	-0.11	0.77	-0.46	-0.93
O	2.13	-0.29	1.83	-0.62	-1.57
OOH	3.64	-0.42	3.22	-0.47	-1.88

References

1 H. C. Tsai, B. Vedhanarayanan and T. W. Lin, *ACS Appl. Energy Mater.*, 2019, **2**, 3708–3716.

2 X. Liu, J. Liu, Y. Li, Y. Li and X. Sun, *ChemCatChem*, 2014, **6**, 2501–2506.

3 P. K. Bhartiya, M. Srivastava and D. Mishra, *Int. J. Hydrogen Energy*, 2022, **47**, 42160–42170.

4 H. Yu, L. Qi, Y. Hu, Y. Qu, P. Yan, T. T. Isimjan and X. Yang, *J. Colloid Interface Sci.*, 2021, **600**, 811–819.

5 X. Wu, T. Dhanasekaran, W. Han, Y. Gao, Y. Li, D. Zhao, G. Wang and J. Zhao, *ACS Appl. Energy Mater.*, 2025, **3**, 158–170.

6 X. Z. Song, T. Zhang, Y. H. Zhao, J. C. Ni, Y. Pan, Z. Tan and X. F. Wang, *Inorg. Chem.*, 2023, **62**, 8347–8356.

7 L. Zeng, L. An, Z. Zhang, J. Zheng, W. Chen, C. Liu, Y. Zheng, D. Dang and Z. Q. Liu, *Chem. Eng. J.*, , DOI:10.1016/j.cej.2024.152084.

8 Y. Zhang, Z. Li, S. He, Y. Qiao, A. Yuan, J. Wu and H. Zhou, *J. Colloid Interface Sci.*, 2025, **679**, 20–29.

9 Q. Qin, H. Jang, L. Chen, G. Nam, X. Liu and J. Cho, *Adv. Energy Mater.*, 2018, **8**, 1–12.

10 F. Diao, W. Huang, G. Ctistis, H. Wackerbarth, Y. Yang, P. Si, J. Zhang, X. Xiao and C. Engelbrekt, *ACS Appl. Mater. Interfaces*, 2021, **13**, 23702–23713.

11 T. Xie, B. Wang, S. Yang, Q. Xu, X. Cheng, C. Zhou and J. Hu, *J. Alloys Compd.*, 2022, **921**, 166111.

12 D. Huo, F. Song, J. Hu, J. Yuan, L. Niu and A. jun Wang, *Int. J. Hydrogen Energy*, 2021, **46**, 8519–8530.

13 A. Gupta, C. A. Allison, A. Kumar, R. Srivastava, M. Sim, J. Horinek, W. Lin, F. M. de Souza, S. R. Mishra, F. Perez, R. K. Gupta and T. Dawsey, *J. Energy Storage*, 2024, **75**, 1–13.

14 G. L. Li, Y. Y. Miao, F. Deng, S. Wang, R. X. Wang, W. H. Lu and R. L. Chen, *J. Colloid Interface Sci.*, 2024, **667**, 543–552.

15 J. O. Silva, S. Cartagena and J. A. Calderón, *Electrochim. Acta*, , DOI:10.1016/j.electacta.2023.142299.

16 J. Chang, Z. Hu, D. Wu, F. Xu, C. Chen, K. Jiang and Z. Gao, *J. Colloid Interface Sci.*, 2023, **638**, 801–812.

17 S. Qiu, S. Hao, Y. Xing, J. Huang, X. Wang, M. Ding, G. Zhao, B. Zhang and Y. Zhang, *Int. J. Hydrogen Energy*, 2022, **47**, 30472–30483.

18 C. Tian, M. Zhang, W. Yan, Y. Qing, L. Li, Y. Wu, J. Li and T. Yang, *Int. J. Hydrogen Energy*, 2023, **48**, 30653–30663.

19 G. Kresse and J. Furthmüller, *Comput. Mater. Sci.*, 1996, **6**, 15–50.

20 J. P. Perdew, K. Burke and M. Ernzerhof, *Phys. Rev. Lett.*, 1996, **77**, 3865–3868.

21 D. Joubert, *Phys. Rev. B - Condens. Matter Mater. Phys.*, 1999, **59**, 1758–1775.

22 S. Grimme, J. Antony, S. Ehrlich and H. Krieg, *J. Chem. Phys.*, , DOI:10.1063/1.3382344.

23 W. Tang, E. Sanville and G. Henkelman, *J. Phys. Condens. Matter*, , DOI:10.1088/0953-8984/21/8/084204.

24 J. K. Nørskov, J. Rossmeisl, A. Logadottir, L. Lindqvist, J. R. Kitchin, T. Bligaard and H. Jónsson, *J. Phys. Chem. B*, 2004, **108**, 17886–17892.

25 V. Wang, N. Xu, J. C. Liu, G. Tang and W. T. Geng, *Comput. Phys. Commun.*, 2021, **267**,

108033.